

Predicting Hemiwicking Dynamics on Textured Substrates

Bharath Natarajan,[§] Aditya Jaishankar,[§] Mark King,[§] Fandi Oktasendra,^{||#} Samuel J. Avis,^{||} Andrew R Konicek,[§] Garrett Wadsworth,[§] Arben Jusufi,[§] Halim Kusumaatmaja,^{||} Mohsen S Yeganeh[§]

[§]Corporate Strategic Research, ExxonMobil Research and Engineering Co., 1545 U.S. 22, Annandale, New Jersey 08801, United States

^{||}Department of Physics, Durham University, Durham, DH1 3LE, United Kingdom

[#]Department of Physics, Universitas Negeri Padang, Padang 25131, Indonesia

KEYWORDS: Hemiwicking, dynamics, wetting, textured surface, liquid transport

ABSTRACT

The ability to predict liquid transport rates on textured surfaces is key to the design and optimization of devices and processes such as oil recovery, coatings, reaction-separation, high-throughput screening, and thermal management. In this work, we develop a fully analytical model to predict the propagation coefficients for liquids hemiwicking through micropillar arrays. This is carried out by balancing the capillary driving force and a viscous resistive force and solving Navier-Stokes' equation for representative channels. The model is validated against a large dataset

of experimental hemiwicking coefficients harvested from literature and measured in-house using high speed imaging. The theoretical predictions show excellent agreement with the measured values, and improved accuracy compared to previously proposed models. Furthermore, using Lattice Boltzmann (LB) simulations, we demonstrate that the present model is applicable over a broad range of geometries. The scaling of velocity with texture geometry, implicit in our model, is compared against experimental data, where good agreement is observed for most practical systems. The analytical expression presented here offers a tool for developing design guidelines for surface chemistry and microstructure selection for liquid propagation on textured surfaces.

Introduction:

Wicking is the spontaneous flow of liquid through an enclosed porous medium driven by capillary action.¹ It is an important surface science phenomenon critical to applications ranging from inkjet printing to liquid hydrocarbon recovery. While wicking broadly describes liquid propagation through a 3D porous medium, hemiwicking is the spreading of a liquid on a textured surface where the wetting of dry regions is accompanied by the increase of liquid-air interfacial area.^{2,3} Interest in hemiwicking was kindled by early studies showing that the addition of texture to smooth substrates significantly enhanced the propagation rates of liquids.^{4,5} A number of groups have investigated the physics underlying such acceleration by textural addition.⁶⁻⁹ For instance, Ueno et al. studied the dynamics of interaction of a planar 3-phase (solid, liquid, air) contact line with a single microparticle. They observed that the wetting of this particle induced the formation of a meniscus at its base and the high capillary pressure (\sim curvature) of this meniscus locally accelerated contact line motion by a factor of 100.⁶ Increased liquid propagation speeds have also been observed for both regular textures⁵ and hierarchical multiscale textures.^{8,9} Interestingly, the

local acceleration and deceleration on textured substrates yields a $\sim t^{1/2}$ (t , time) scaling with macroscopic propagation distance (z). In contrast the spreading distance on a flat, smooth surface is known to follow Tanner’s law, $z \sim t^{1/10}$.⁷ As evidence of this scaling difference, Quere *et al.* noted that while a water droplet of 1 mm diameter takes 10 days to spontaneously spread to 2 mm on a smooth substrate, with the addition of appropriate texture this process is achieved in as little as 10 s.¹⁰

Recent advancements in nano-/micro-patterning technology have enabled the fabrication of textures with tunable wettability and transport properties. These developments enabled applications exploiting hemiwicking in thermal management,¹¹ liquid-infused surfaces,^{12, 13} energy harvesting,¹⁴ and lab-on-a-chip devices.^{15, 16} The patterned textures have also allowed the investigation of interesting flow behavior such as zipping,¹⁷ anisotropic/polygonal spreading^{18, 19} and large rise heights.²⁰ However, further utilization of fast hemiwicking dynamics in commercial applications requires a quantitative understanding of the role of complex liquid-solid interactions that dictate liquid propagation and wetting. Specifically, the ability to predict liquid transport rates at the macroscopic scale will enable the design and optimization of textures for high performance liquid infusion applications.²¹⁻²³

In the 20th century Bell, Cameron,^{24, 25} Lucas, and Washburn²⁶ recognized that flow through porous media followed the “diffusive” scaling law, $z = (Dt)^{\frac{1}{2}}$, where z is the wicked distance, t is the time, and D is a propagation coefficient determined by the relative strengths of the capillary driving force and viscous resistance.²⁷ For flow through a cylindrical tube, D is a function of the diameter, d , given by $D = \frac{\gamma d \cos \theta}{4\mu}$, where γ is the liquid-vapor surface energy, θ is the equilibrium contact angle of the liquid on a smooth surface made from the same solid, and μ is the liquid

viscosity. However, for hemiwicking through a texture, D must be described by a more complex function involving at least three geometrical parameters. There have been several efforts (Table S1) to arrive at a functional form of D for hemiwicking by incorporating the geometric parameters of textured surfaces into models for capillary pressure and viscous resistance.^{2, 10, 28-31} We note that either for the sake of simplicity or as demanded by the end use, the textured substrates used in these studies have primarily been periodic micropillar arrays. These arrays are constituted of pillars of square or circular cross section arranged in patterns with a characteristic periodicity or pitch, p .^{2, 10, 28-31}

The seminal work by Ishino and Quere *et al.* identified two structural regimes in which dissimilar scaling behaviors were observed owing to different dominant dissipative phenomena.¹⁰ For short and long pillar heights, h , relative to the pitch, p , viscous friction was shown to be dominated by either the bottom surface ($h \ll p$) or the pillars ($h \gg p$) themselves, respectively. However, the boundaries between these regimes were not clarified and a model describing behavior in the broad $h \approx p$ regime was lacking. Srivastava *et al.* developed a semi-analytical scaling model that used dimensional analysis and finite element simulations to estimate the viscous resistance around a single cylindrical pillar.²⁹ While this approach is fruitful, the presented model is only valid for a specific pillar geometry and in the design space where multipillar effects are negligible. Qiao *et al.* have demonstrated an empirical model that estimates capillary pressure more accurately by simulating the meniscus shape using Surface Evolver (SE).^{30, 31} The viscous resistance was obtained by solving a modified form of the Stokes' equation. This model was noted to be best suited for pillar arrays with a diameter to pitch ratio (d/p) less than 0.57. Further, for sparse arrays, additional corrections based on microscale wicking phenomena were required. This approach, being semi-analytical, also necessitates significant new model development for new

array geometries. Kim *et al.*²⁸ and Krishnan *et al.*³² have demonstrated models that capture the velocity scaling appropriately, but their models are found to require a fitting factor to match measured D values. While other hemiwicking models have been suggested, Kim *et al.* have demonstrated that these other models do not capture the scaling behavior correctly.²⁸ In summary, previously suggested forms of the hemiwicking coefficient are only accurate under limited conditions.²⁸ Additionally, the breadth of applicability of certain models is restricted by the semi-analytical or empirical nature of their approach.²⁹⁻³² A universal analytical model to accurately predict liquid propagation rates on patterned surfaces is thus far absent.

In this work, we sought to build a predictive model that is simple, accurate, and is broadly applicable to textured surfaces that contain various pillar geometries, patterns, and relative dimension scale. Our model balances the capillary pressure, described previously by Quere *et al.*,³ with the viscous resistance estimated by solving Stokes' equation for a rectangular channel. The size of the channel is appropriately selected to capture the frictional contribution of the array geometry. Our model provides an analytical expression that accurately predicts the hemiwicking coefficient for a wide range of textured geometry generated by micropillars. The final expression is validated using extensive data published by others and as well as new measurements captured with high speed imaging. In addition, we employed Lattice Boltzmann (LB) simulations to further show that the present model is accurate over a much broader range of micropillar geometries compared to previously published models. Our model also correctly predicts the scaling of D with the geometric parameters describing the micropillar array.

Methods

Model Development

Consider a micropillar array of roughness factor, r , which is the ratio of the total solid surface area to the 2D projected area. We define the purely imbibed state³³ as the texture filled while the tops of the pillars remain dry,^{28, 33} with φ_s as the ratio of the dry pillar top area to the projected area. The criterion for hemiwicking into such an array was derived by Bico *et al.*³⁴ to be (see supporting information)

$$\cos \theta \geq \frac{(1 - \varphi_s)}{(r - \varphi_s)} = \cos \theta_c \quad (1)$$

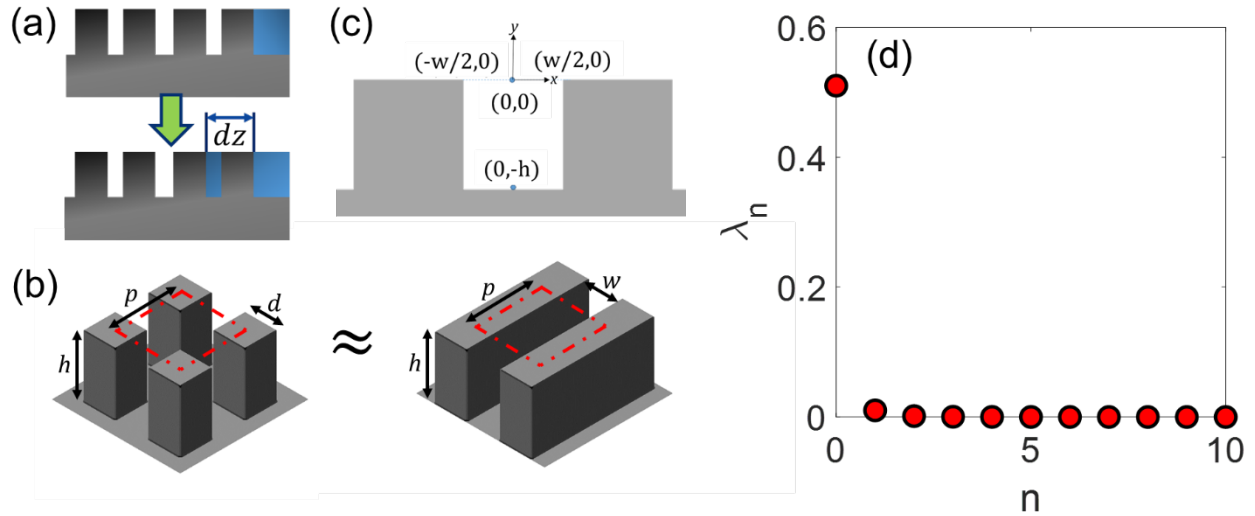


Figure 1. (a) Illustration of hemiwicking process through a micropillar array, highlighting the assumption of a flat meniscus and coplanarity between the meniscus and tops of the pillars. (b) Illustration demonstrating the approximation approach employed to calculate viscous dissipation. The width of the rectangular open channel (w) is modified to ensure that the volume of liquid contained in the unit cell areas are identical. (c) Schematic showing the coordinate system used in the derivation of the flow profile. (d) Plot of the term in the summation in Eq. (10) (λ_n), against n for $h = 10 \mu\text{m}$ and $w = 25 \mu\text{m}$.

Equation (1) identifies a critical contact angle, θ_c , defined by the texture geometry. Hemiwicking is favored for all inherent contact angles smaller than θ_c . We note here that this model assumes a flat liquid meniscus and coplanarity between the meniscus and the top of the pillar, see Figure 1(a). For super hydrophilic substrates (where contact angle $\theta = 0^\circ$ and the spreading coefficient $S \geq 0$) the pillars tops are also wet at equilibrium. However, during wicking, the velocity of the wicking front far exceeds the rate of spreading of a liquid film on the pillar tops.²⁸ Therefore, in our calculations we consider the pillar tops as being dry. In Eq. (1), for any surface with texture, r is always greater than 1 and φ_s is less than 1. Thus, θ_c is between 0° and 90° , where 0° is the critical contact angle for spreading on a flat plane ($r \rightarrow 1$) and 90° is the critical angle of wicking in porous media ($r \rightarrow \infty$).

In hemiwicking the Reynolds numbers ($Re = \rho U p / \mu$, where ρ is the density, U is the velocity, μ is the viscosity, and p is the pillar-pillar distance or pitch) are small ($\sim 10^{-4}$) and hence inertial effects are negligible. Additionally, the Bond numbers ($Bo = \rho h^2 g / \gamma_{LV}$, where g is the acceleration due to gravity, γ_{LV} is the liquid-vapor surface tension, and h is the pillar height) are small as well ($\sim 10^{-5}$), indicating gravitational forces can be ignored. Therefore, when the hemiwicking criterion in Equation (1) is satisfied, the rate of wicking of liquid into the texture is simply dictated by the balance between a driving capillary pressure (ΔP_L) and a dissipative Darcy-like viscous pressure (ΔP_V), resulting in the scaling law, $z = (Dt)^{\frac{1}{2}}$. ΔP_L is the change in interfacial free energy per unit volume of liquid wicked. This derivation leads to Eq. (2) (details are in the supporting information).

$$\Delta P_L = \frac{\gamma_{LV}}{h} \left(\frac{\cos \theta - \cos \theta_c}{\cos \theta_c} \right) \quad (2)$$

As is evident and in agreement with Eq. (1), the capillary pressure (the only hemiwicking driving force) is only positive when the $\theta \leq \theta_c$. The viscous dissipation force per unit area or viscous pressure (ΔP_V) can be estimated,² from a modification to the classical Poiseuille law for a liquid film of thickness, h , flowing on a plane.¹⁰

$$\Delta P_V = \frac{3\mu\bar{U}z}{h^2} \beta \quad (3)$$

where \bar{U} is the average velocity of propagation (dz/dt) and β is a correction factor to the classical Poiseuille law that accounts for enhanced dissipative contributions from the microtexture. h here is the same as the pillar height, as during hemiwicking the top of the liquid volume is pinned/confined to the top edge of the pillar.^{28,33} Balancing the capillary pressure and viscous pressures leads to

$$z^2 = \frac{2\gamma_{LV}h}{3\mu} \left(\frac{\cos \theta - \cos \theta_c}{\cos \theta_c} \right) \frac{1}{\beta} t \quad (4)$$

Comparing to Eq. (4), the hemiwicking coefficient is thus

$$D = \frac{2\gamma_{LV}h}{3\mu} \left(\frac{\cos \theta - \cos \theta_c}{\cos \theta_c} \right) \frac{1}{\beta} \quad (5)$$

For a given liquid, a substrate chemistry, and textured geometry all parameters in Eq. (5) are known except for β . β can be experimentally determined; however, experimental investigation of the effect of the array geometry on the correction factor is tedious and precludes the development of a model to fully theoretically predict the value of D .

To do so, we take inspiration from Hay *et al.*³⁵ and Mai *et al.*³⁶, approximating the flow of liquid through the micropillar array as flow through an equivalent microchannel (Figure 1b). Here, the channel is set to have the same wall height, h , in order to elucidate the role of this geometric

parameter. However, the width of the channel, w , is modified to ensure that the maximum volume available per unit length (volume/ p) is identical between the two systems. The validity of this volume approximation is explained from a hydraulic resistance viewpoint in the supporting information (Figure S1). For example for a square array of square cross-section pillars $w = \frac{(p^2 - d^2)}{p}$, where d is the side of the square and p is the pitch.

The velocity of the liquid through said microchannel can be obtained by solving Stokes' equation for steady-state, parallel, incompressible flow.

$$-\frac{\Delta P_L}{\mu z} = \frac{\partial^2 U}{\partial x^2} + \frac{\partial^2 U}{\partial y^2} \quad (6)$$

where, $U(x, y)$ is the velocity profile in the microchannel. We assume no slip on the microchannel walls, *i.e.*, the velocity at the walls is zero and free slip at the top surface. By solving the equation using these boundary conditions (details of the solution are in the supporting information), we obtain the velocity profile in the microchannel as

$$U(x, y) = \frac{16\Delta P_L h^2}{\mu z \pi^3} \sum_{n=0}^{\infty} \frac{(-1)^n}{(2n+1)^3} \left(1 - \frac{\cosh\left[\frac{(2n+1)\pi x}{2h}\right]}{\cosh\left[\frac{(2n+1)\pi w}{4h}\right]} \right) \cos\left[\frac{(2n+1)\pi y}{2h}\right] \quad (7)$$

and the spatially-averaged velocity (mean velocity) at a given distance z along the channel length is

$$\bar{U} = \frac{1}{wh} \int_{-w/2}^{w/2} \int_{-h}^0 U(x, y). dx. dy \quad (8)$$

$$\bar{U} = \frac{32\Delta P_L h^2}{\mu z \pi^4} \sum_{n=0}^{\infty} \frac{1}{(2n+1)^4} \left(1 - \frac{4h}{(2n+1)\pi w} \tanh \left[\frac{(2n+1)\pi w}{4h} \right] \right) = \frac{32\Delta P_L h^2}{\mu z \pi^4} \sum_{n=0}^{\infty} \lambda_n \quad (9)$$

In Eq. (9), due to the $\frac{1}{(2n+1)^4}$ dependence, the value of the terms in the summation (λ_n) become negligibly small for $n \geq 1$ (Figure 1d). Therefore the mean velocity can be approximated as

$$\bar{U} \approx \bar{U}_{n=0} C = C \frac{32\Delta P_L h^2}{\mu z \pi^4} \left(1 - \frac{4h}{\pi w} \tanh \left[\frac{\pi w}{4h} \right] \right) \quad (10)$$

where C is a correction factor to account for the contributions from the $n > 0$ terms. To obtain the value of C , we compare the mean velocity obtained here for $w \rightarrow \infty$ against the Poiseuille flow velocity over a flat plane. Ideally, these two scenarios are equivalent.

$$C \frac{32\Delta P_L h^2}{\mu z \pi^4} = \frac{\Delta P_L h^2}{3\mu z} \quad (11)$$

$$C = \frac{\pi^4}{96} \approx 1.014 \quad (12)$$

The above indicates that the correction term is only slightly larger than 1, showing that the contribution from the $n > 0$ terms is very small. From Eq. (10) and Eq. (11), we obtain

$$\bar{U} = \frac{\Delta P_L h^2}{3\mu z} \left(1 - \frac{4h}{\pi w} \tanh \left[\frac{\pi w}{4h} \right] \right) \quad (13)$$

Using Eq. (3), substituting for ΔP_L in Eq. (14) leads to

$$\bar{U} = \frac{\gamma_{LV} h}{3\mu z} \left(\frac{\cos \theta - \cos \theta_c}{\cos \theta_c} \right) \left(1 - \frac{4h}{\pi w} \tanh \left[\frac{\pi w}{4h} \right] \right) \quad (14)$$

Comparing Eq. (14) and Eq. (5), we find

$$\beta = \frac{1}{1 - \frac{4h}{\pi w} \tanh\left[\frac{\pi w}{4h}\right]} \quad (15)$$

In Eq. (15), as the denominator is always less than one, the correction term to the viscous force is always greater than one, showing that more texture leads to more viscous dissipation. From Eq. (14) and the “diffusive” scaling law, the hemiwicking coefficient is thus

$$D = \frac{2\gamma_{LV}h}{3\mu} \left(\frac{\cos\theta - \cos\theta_c}{\cos\theta_c} \right) \left(1 - \frac{4h}{\pi w} \tanh\left[\frac{\pi w}{4h}\right] \right) \quad (16)$$

The equation in this form is not dependent on any specific geometry. The adaptation, as well as the validation (Figure S2) of Eq. (16) to specific geometries is demonstrated in the supporting information.

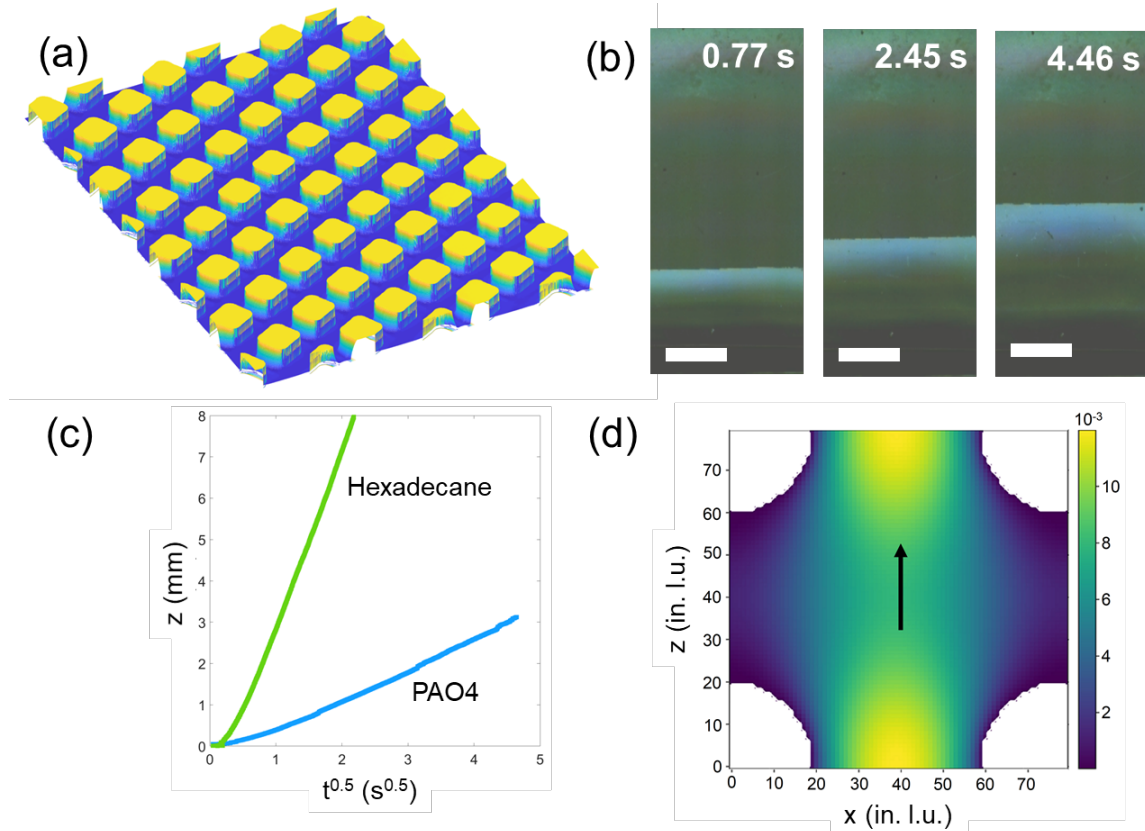


Figure 2. (a) 3D rendering of optical profilometry data obtained on the micropillar array (color scale refers to height; texture pitch = 20 μm , square cross-section side length = 10 μm , and pillar

height = 7 μm) used in our hemiwicking experiments. (b) Snapshots from high speed video (top view of array) of hexadecane hemiwicking through the array in (a). Scale bar represents 2.5 mm. (c) Plot of hemiwicked distance versus time to the one half power for hexadecane and polyalphaolefin-4 (PAO4) on our micropillar array. (d) Top view of LB simulated velocity profile in a representative unit cell of a cylindrical micropillar array; all values are represented in simulation units. When translated to experimental data the array dimensions (height = 26 μm , diameter = 10 μm , pitch = 20 μm) represent those in Kim et al.²⁸ The color bar represents velocity and the direction of propagation is indicated by the arrow.

High speed imaging: Hemiwicking experiments were performed using a silicon micropillar array with a pitch of 20 μm , a square cross-section of side 10 μm , and a pillar height of 7 μm , as measured by optical profilometry (Figure 2a). This array of size 1.5 cm \times 1.5 cm, was mounted vertically onto a micrometer stage and was brought into contact with a reservoir of the hemiwicking liquid (Figure 2b). Three hemiwicking fluids of nearly identical surface tensions but varying viscosities were employed (See Table S2). The macroscale hemiwicking process was observed using a Photron FASTCAM SA1.1 high speed camera, fitted with an Infiniprobe TS-160 macro lens and pointed normal to the texture surface, capturing images at a frame rate of 500 frames/second. The Photron FASTCAM Viewer software was used to capture the videos. The hemiwicking videos were image processed and thresholded using ImageJ and the wicking front was tracked as a function of time. The square of the slope of the distance versus time to the one half power is reported as the hemiwicking coefficient, D (Figure 2c).

Lattice Boltzmann Simulation

In this work, we do not explicitly simulate the hemiwicking dynamics. Instead, to obtain the propagation coefficient D , it is sufficient to solve the flow profile for a unit cell of the micropillar array. We carry this out using a standard LB method with a D3Q19 velocity set,³⁷ and the typical flow profile is shown in Figure 2(d). To mimic the capillary pressure, we apply a body force $f =$

$-\Delta P_L/z$ to the fluid, following the definition of the capillary pressure in Eq. (2) and the Stokes' equation in Eq. (6).

The unit cell consists of a single square or cylindrical pillar, with periodic boundary conditions applied on the sides of the unit cell. Typically, we use a simulation box of $p \times p \times h$ (all in lattice units), in which the pitch p is always set to 50 lattice units and the pillar height h is varied between 8 and 100 lattice units. The post diameter d is also varied between 8 and 40 lattice units. These variations in h and d allow us to construct contour plots in terms of p/h and p/d . A no-slip boundary condition for the solid-liquid interfaces is implemented using a bounce-back boundary condition. To represent the liquid-gas interface at the upper boundary of the unit cell a free slip boundary condition is employed. The effect of curved liquid-gas interface is not included.

From the flow profile we are able to compute the average fluid velocity in the unit cell, \bar{U} . Balancing Eq. (14) and Eq. (16), we can then express the simulated D value in terms of \bar{U} , the capillary pressure ΔP_L , and the applied body force f

$$D = 2\bar{U} \frac{-\Delta P_L}{f} \quad (17)$$

Results and Discussion:

Model Validation

To validate our model, we compare the hemiwicking coefficient values predicted by Eq. (17) against experimental data obtained in house (labelled as ‘‘This Study’’) and those values reported in literature.^{10, 28, 30, 31, 36} The harvested values comprised ~ 45 data points spanning square and cylindrical pillar geometries, with pillar densities ranging from $p > h$, $p \approx h$, and $p < h$.^{10, 28, 30, 31,}

³⁶ Figure 3a shows the comparison between the internal and externally measured D and the values

predicted by our model. Fig. 3b displays the comparison between the same experimental results and the values obtained by models generated in previous works. The proximity of our predictions to the slope of 1 in Figure 3a demonstrates the ability of Eq. (16) to accurately determine the experimentally obtained hemiwicking coefficients over a wide range of values (~ 0.05 to $170 \text{ mm}^2/\text{s}$). The root mean square error in prediction is calculated to be 0.28 (Table S1). As is evident from our model development, we do not consider the effect of pinning/depinning phenomena, such as those described by Blow and Yeomans.³⁸ This is because we are primarily focused on low equilibrium contact angle systems that favor rapid liquid transport. At these angles (Table S2) pinning effects are noted to be negligible.³⁸

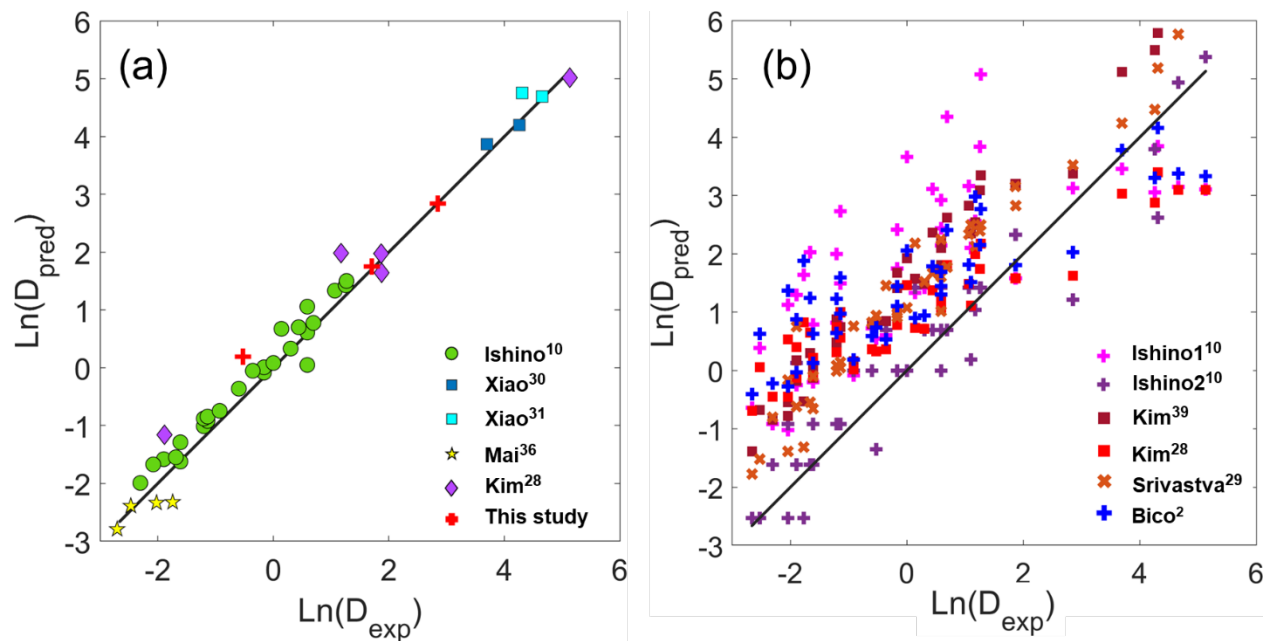


Figure 3. Both plots in log-log scale. (a) Plot of the D values predicted by our model against the experimentally measured D values.^{10, 28, 30, 31, 36} (b) Plot of the D values predicted by *other* models^{2, 10, 28, 29, 39} against the experimentally measured D values.

We note that the range of geometries in the curated data is limited to p/h values between 0.14 and 3.3 and the majority of p/d values between 1.5 and 4. To probe the breadth of applicability of our model we performed LB simulations over an extensive range of geometries. In all cases, we

assume a contact angle of 0° in the definition of the capillary pressure. Firstly, the LB simulations were validated, as demonstrated by the close agreement between simulated values and the experimental data for the curated geometries (Figure S3). Then extensive LB simulations were conducted for cylindrical pillar geometries with p/h values from 0.5 to 10 and p/d values between 1.25 and 6.25. The D values measured from these simulations were then compared against those predicted by our analytical expression in Eq. (16) and the absolute error percentage is plotted as a function of geometry in Figure 4. We note that over a broad range of geometries the absolute error is within 30%. This represents a reasonable error value allowing for uncertainties in measuring viscosity, surface tension, geometry, hemiwicking rate, as well as inter- and intra-sample non-uniformities. The model appears to deviate from the predicted values in the region where the pitch is comparable to the diameter, *i.e.*, in very dense arrays. The deviation, in this regime, is due to the confinement of the flow primarily within the narrow gap between the pillars. Hence, the effective width, w , becomes smaller than our current assumption for the equivalent microchannel in Figure 1b. That said, the highly dense arrays do not represent practically useful geometries as available flow through the narrow spaces is much reduced.

Having demonstrated the prediction accuracy of D values for a wide range of geometries, we now discuss how the limitation of prior models were addressed. We limit our discussion to models that present an expression for D .^{2, 10, 28, 29, 39} A subset of previously suggested models are limited by the assumption that frictional contributions are dominated by specific textural features. For example, the Bico² and Ishino models¹⁰ assume drag to arise from the array base alone. Another model by Ishino et al.¹⁰ assumes friction from only the pillar side-walls. These assumptions result in the over-prediction of D as the viscous losses are underestimated (Figure 3b). While such exclusive contributions to viscous dissipation are likely in extreme scenarios

where $p \ll h$ or $p \gg h$, in all intermediate situations ($p > h$, $p \approx h$, $p < h$) combined contributions from the base and pillars need to be accounted for. By approximating the array to a channel, we explicitly consider frictional contribution from both the walls and the base, resulting in closer predictions. From Figure 4, we note that the Ishino models¹⁰ appear to predict well in a band of intermediate p/h and p/d , which is mainly within our domain of accuracy, as well as when p/h and p/d are very small. These extremes are where Ishino *et al.*'s assumptions are appropriate.¹⁰

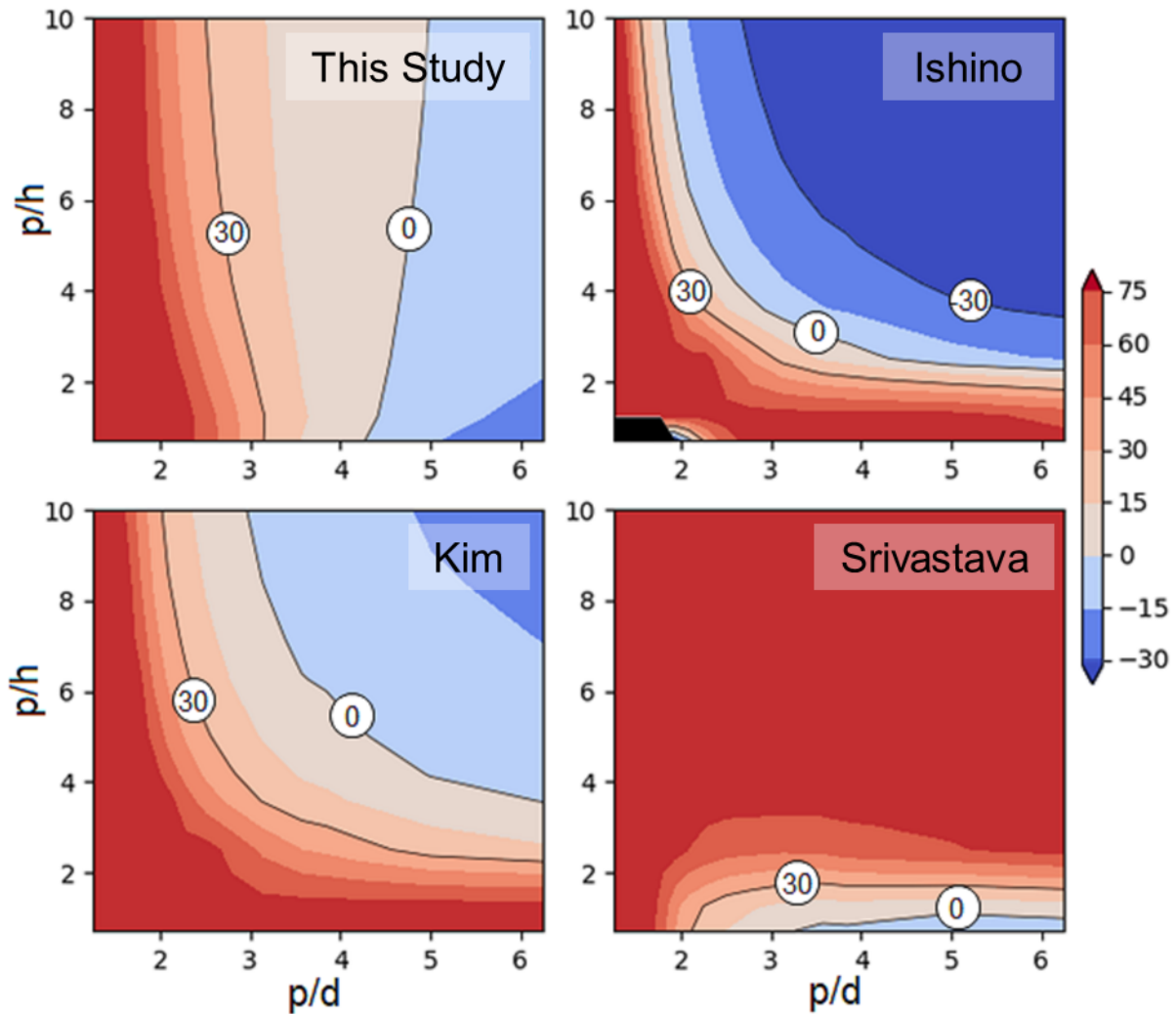


Figure 4. Contour plot of error (%) as a function of pitch/diameter and pitch/height for the model developed in this work (top-left), the Ishino model (top-right),¹⁰ the Kim model²⁸ (bottom-left) and

the Srivastava model²⁹ (bottom-right). Several percentage errors are indicated in the plots. We note that the Ishino model for $p < h$ is constrained by $\ln(p/d) > 1.31$, beyond which the D values become unphysical (negative). This is indicated by the black area in the bottom left corner of the Ishino panel. The error shown here is the difference between the simulated and model predicted value over the simulated value, expressed in percentages.

Other models are limited by how they reduce the texture into very simplistic representative elements. Srivastava *et al.* presented a semi-analytical model where the viscous dissipation was estimated using finite element (FE) modeling of flow around a single pillar.²⁹ By repeating this analysis for various geometries, the authors derived the scaling law shown in Table S1. From Figure 3b it is apparent the Srivastava model, which requires a fitting parameter, consistently over predicts ($\sim 3\times$) D values. We attribute this mismatch in predicted and measured values to the exclusion of multipillar effects in their single pillar FE simulations. As noted earlier, multipillar effects are implicitly captured in our model by the channel walls. In line with this argument, we note from Figure 4 that the Srivastava model²⁹ predicts well for tall pillars with $p/d > 2$, where drag from side walls dominates the dissipation and multi-pillar effects are diminished.

More recent models have considered the arrays in their full complexity (Kim *et al.*²⁸) and have further argued for the explicit consideration of the extension length of the wicking front (Krishnan *et al.*³²). These models predict scaling correctly for a broad range of geometries. However, they require empirically determined correction factors to accurately predict the velocity (see Table S1) and are applicable only in the superhydrophilic limit ($\theta = 0^\circ$). The empirical nature of these recent models limits their universality. In contrast, our model demonstrates the capability to predict the absolute value of the hemiwicking coefficient in an ab-initio fashion. That said, with a fitting factor applied (~ 0.24), the Kim model is shown to predict the data closely (Table S1). Further from Figure 4, we observe that the envelope of good prediction quality (absolute error $<$

30%) for the Kim model²⁸ (fitting factor applied) extends further into the regime where p/d is small and p/h is large when compared with our model.

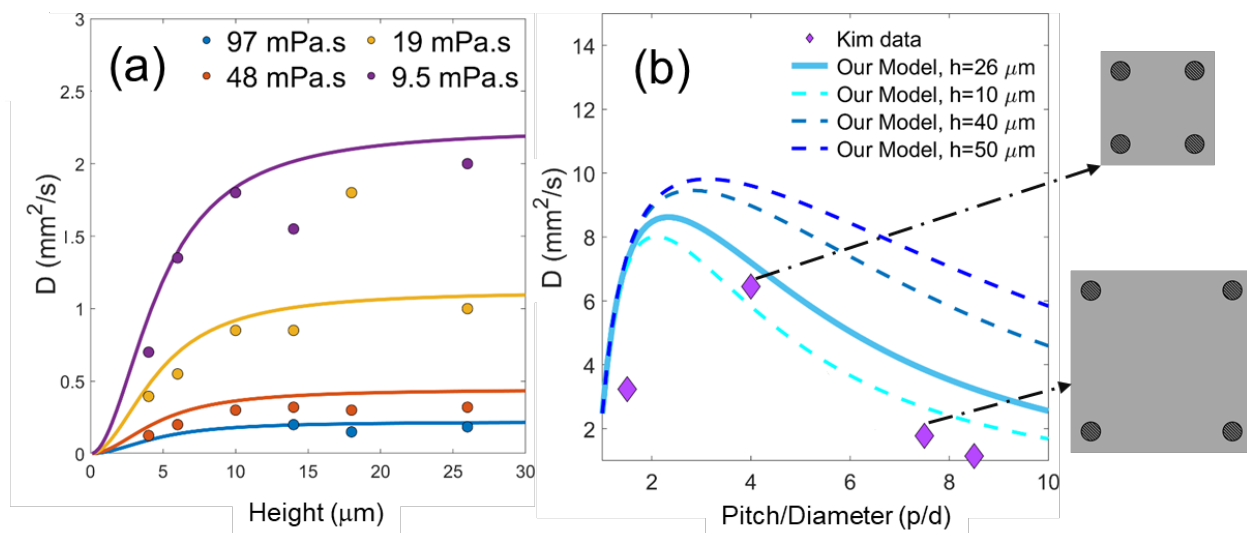


Figure 5. (a) Plot of hemiwicking coefficient (D) versus the height of pillars for liquids of various viscosities. The following parameters are not modified: cylindrical cross section, pitch = $10 \mu\text{m}$, diameter = $2.6 \mu\text{m}$, $\gamma_{LV} = 20 \text{ mN/m}$, contact angle = 0° . The circles represent the experimentally measured data by Ishino *et al.*¹⁰ and the lines represent the predictions by our analytical expression. (b) Plot of hemiwicking coefficient (D) versus the ratio of pitch to diameter for various pillar heights. The following parameters are not modified: cylindrical cross section, diameter = $10 \mu\text{m}$, $\gamma_{LV} = 48 \text{ mN/m}$, $\mu = 18 \text{ mPa}\cdot\text{s}$, contact angle = 0° . The schematics show the top view of a unit cell of the pillar lattice, highlighting the extreme case of high p/d values.

We then investigated the velocity scaling predicted by our model. Figure 5a shows a plot of the dynamic coefficient versus height for a square array of cylindrical pillars of diameter $2.6 \mu\text{m}$ for liquids of various viscosities, all with a contact angle of 0° . These parameters are chosen because they represent the conditions for the experiments reported by Ishino *et al.*, where heights and viscosities are varied systematically while keeping all other parameters identical (cylindrical cross section, pitch = $10 \mu\text{m}$, diameter = $2.6 \mu\text{m}$, $\gamma_{LV} = 20 \text{ mN/m}$, contact angle = 0°).¹⁰ We further note that D increases steeply with height for small heights and reaches a saturation value quickly. Further, at very small heights ($h \sim 0.1p$), D appears to bear a quadratic relationship with height. For a square array with cylindrical pillars and a contact angle of 0° , Eq. (16) can be written as,

$$D = \frac{2\gamma_{LV}h}{3\mu} \left(\frac{\pi dh}{(p^2 - \pi d^2/4)} \right) \left(1 - \frac{4ph}{\pi(p^2 - \pi d^2/4)} \tanh \left[\frac{\pi(p^2 - \pi d^2/4)}{4ph} \right] \right). \quad (18)$$

Here, when $p \gg h$, $\frac{4ph}{\pi(p^2 - \pi d^2/4)} \ll 1$, and $\tanh \left[\frac{\pi(p^2 - \pi d^2/4)}{4ph} \right] \sim 1$. Therefore, the term in the parenthesis in Eq. (18), becomes ~ 1 . Thus,

$$D = \frac{2\pi\gamma_{LV}d}{3\mu(p^2 - \pi d^2/4)} h^2 \sim h^2. \quad (19)$$

This scaling is in agreement with Ishino *et al.*'s model that suggests a quadratic relationship with h for $h \ll p$ and minimal dependence on h when $h \gg p$. However, in the intermediate scenarios, we observe deviations from these dependences. Further, barring some outliers, we note excellent agreement between the experimental data and our predictions (Figure 5a), indicating that the scaling with h implicit in our expression is correct.

In Figure 5b, we plot the hemiwicking coefficient scaling as a function of the pitch over the pillar diameter (p/d), as predicted by our model. Starting from a ratio of 10, with decreasing p/d , D increases, reaches a peak value before decreasing for low p/d values. This trend is in general agreement with models proposed earlier. This reduction after a peak p/d is because with further texture addition, viscous resistance grows more strongly than capillary driving force. From model plots for other heights, we note that the p/d value for the maximum D is relatively insensitive to the texture height. On Figure 5b we also plot data from Kim *et al.*,²⁸ who systematically varied the pitch, while keeping all other parameters identical (cylindrical cross section, height = 26 μm , diameter = 10 μm , $\gamma_{LV} = 48$ mN/m, $\mu = 18$ mPa·s, contact angle = 0°). From the Figure 5b we observe that there is reasonable quantitative and qualitative agreement with the scaling up to a p/d of ~ 4 . At higher p/d , the measured D decreases more rapidly than the predicted value. This is likely

because conduit models such as ours do not work well for high porosity geometries where friction drag of flow around objects dominates over viscous resistance. However, arrays with such large spacing only permit highly wetting liquids (see wetting criterion in (6), Figure 5b) and represent an extreme case of the arrays used for liquid transport, as flow is not much accelerated.

In summary, we have demonstrated an analytical model that accurately predicts the hemiwicking coefficient for macroscale liquid transport on textured surfaces with regular pillar arrays. We note that no experimental fitting factors are necessary to improve the prediction quality. Furthermore, no explicit consideration of microscale wicking phenomena such as zipping or meniscus extension was required. The effects of pinning were also not considered in this work, as the systems studied here are highly wetting (in favor of rapid wicking) and the equilibrium contact angles are well below the lower bound of depinning critical angles.³⁸ The derived expression is demonstrated to be flexible and accurate predictions are obtained over a broad range of textural densities for cylindrical and square pillars. We believe our model can be extended to other pillar shapes as long as the contact angles remain low, and it will be interesting to verify this in the future. The model is observed to breakdown in the extreme case of $p > 4d$ where drag (neglected here) plays an enhanced role, and in the case of small p/d where the flow is confined in the narrow gap between the pillars as demonstrated by LB simulations. Nevertheless, we believe that this work sheds light on complex interfacial interactions that dictate spreading behavior in practically useful textured surfaces.

ASSOCIATED CONTENT

Supporting Information. The following files are available free of charge.

Detailed derivation of hemiwicking model and table with experimental data. (PDF)

AUTHOR INFORMATION

Corresponding Author

Bharath Natarajan, bharath.natarajan@exxonmobil.com

Author Contributions

The manuscript was written through contributions of all authors. All authors have given approval to the final version of the manuscript.

ACKNOWLEDGMENT

The authors would like to thank Dr. Jevan Furmanski for his guidance with optical imaging. FO acknowledges a BPPLN scholarship from the Directorate General of Resources for Science Technology and Higher Education, Republic of Indonesia. SJA is supported by a studentship from the Engineering and Physical Sciences Research Council.

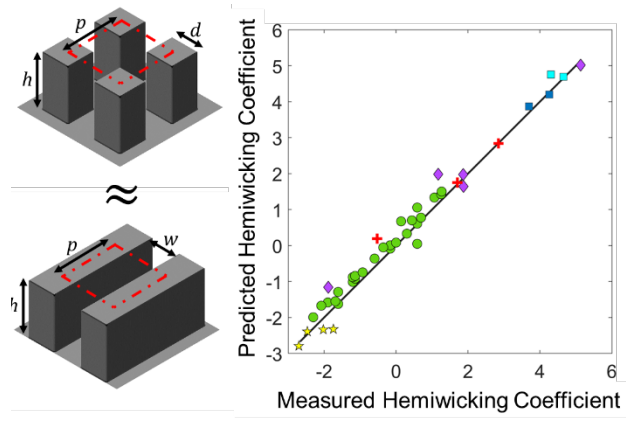
REFERENCES

1. Raux, P. S.; Cockenpot, H.; Ramaioli, M.; Quéré, D.; Clanet, C. J. L., Wicking in a Powder. *Langmuir* **2013**, *29* (11), 3636-3644.
2. Bico, J.; Thiele, U.; Quere, D., Wetting of textured surfaces. *Colloid Surface A* **2002**, *206* (1-3), 41-46.
3. Quere, D., Rough ideas on wetting. *Physica A* **2002**, *313* (1-2), 32-46.
4. McHale, G.; Shirtcliffe, N. J.; Aqil, S.; Perry, C. C.; Newton, M. I., Topography Driven Spreading. *Physical Review Letters* **2004**, *93* (3).

5. Hale, R. S.; Ranjan, R.; Hidrovo, C. H., Capillary flow through rectangular micropillar arrays. *International Journal of Heat and Mass Transfer* **2014**, *75*, 710-717.
6. Mu, L.; Yoshikawa, H. N.; Zoueshtiagh, F.; Ogawa, T.; Motosuke, M.; Ueno, I., Quick Liquid Propagation on a Linear Array of Micropillars. *Langmuir* **2019**, *35* (28), 9139-9145.
7. Nakamura, H.; Ogawa, T.; Inoue, M.; Hori, T.; Mu, L.; Yoshikawa, H. N.; Zoueshtiagh, F.; Dietze, G.; Tsukahara, T.; Ueno, I., Pumping effect of heterogeneous meniscus formed around spherical particle. *Journal of Colloid and Interface Science* **2020**, *562*, 133-141.
8. Rokoni, A.; Kim, D.-O.; Sun, Y., Micropattern-controlled wicking enhancement in hierarchical micro/nanostructures. *Soft matter* **2019**, *15* (32), 6518-6529.
9. Shrestha, R.; Yu, B.; Yang, Q.; Gong, W.; Shen, S., Hierarchical Micro-Nanostructured Surfaces for Isotropic/Anisotropic Liquid Transport. *Langmuir* **2020**, *36* (6), 1569-1573.
10. Ishino, C.; Reyssat, M.; Reyssat, E.; Okumura, K.; Quere, D., Wicking within forests of micropillars. *Epl-Europhys Lett* **2007**, *79* (5).
11. Kim, B. S.; Lee, H.; Shin, S.; Choi, G.; Cho, H. H., Interfacial wicking dynamics and its impact on critical heat flux of boiling heat transfer. *Applied Physics Letters* **2014**, *105* (19).
12. Wong, T. S.; Kang, S. H.; Tang, S. K.; Smythe, E. J.; Hatton, B. D.; Grinthal, A.; Aizenberg, J., Bioinspired self-repairing slippery surfaces with pressure-stable omniphobicity. *Nature* **2011**, *477* (7365), 443-7.
13. McHale, G.; Orme, B. V.; Wells, G. G.; Ledesma-Aguilar, R., Apparent Contact Angles on Lubricant-Impregnated Surfaces/SLIPS: From Superhydrophobicity to Electrowetting. *Langmuir* **2019**, *35* (11), 4197-4204.
14. Ismail, K.; Abogderah, M., Performance of a heat pipe solar collector. *Journal of Solar Energy Engineering* **1998**, 51-59.
15. Cui, H. H.; Lim, K. M., Pillar Array Microtraps with Negative Dielectrophoresis. *Langmuir* **2009**, *25* (6), 3336-3339.
16. Nagrath, S.; Sequist, L. V.; Maheswaran, S.; Bell, D. W.; Irimia, D.; Ulkus, L.; Smith, M. R.; Kwak, E. L.; Digumarthy, S.; Muzikansky, A.; Ryan, P.; Balis, U. J.; Tompkins, R. G.; Haber, D. A.; Toner, M., Isolation of rare circulating tumour cells in cancer patients by microchip technology. *Nature* **2007**, *450* (7173), 1235-U10.
17. Sbragaglia, M.; Peters, A. M.; Pirat, C.; Borkent, B. M.; Lammertink, R. G.; Wessling, M.; Lohse, D., Spontaneous breakdown of superhydrophobicity. *Physical Review Letters* **2007**, *99* (15), 156001.
18. Courbin, L.; Denieul, E.; Dressaire, E.; Roper, M.; Ajdari, A.; Stone, H. A., Imbibition by polygonal spreading on microdecorated surfaces. *Nature Materials* **2007**, *6* (9), 661-664.
19. Vrancken, R. J.; Blow, M. L.; Kusumaatmaja, H.; Hermans, K.; Prenen, A. M.; Bastiaansen, C. W.; Broer, D. J.; Yeomans, J. M., Anisotropic wetting and de-wetting of drops on substrates patterned with polygonal posts. *Soft Matter* **2013**, *9* (3), 674-683.
20. Chu, K. H.; Xiao, R.; Wang, E. N., Uni-directional liquid spreading on asymmetric nanostructured surfaces. *Nature Materials* **2010**, *9* (5), 413-417.
21. Mohsen S. Yeganeh, M. S. I., Shane P. Deighton, Michael Siskin, Aditya Jaishankar, Charles Maldarelli, Pedro Bertolini, Andrew R. Konicek, Bharath Natarajan, Jessica L. Vreeland, Arben Jusufi, Structuring liquid using functionalized surfaces for effective carbon capture. *Submitted to Nature* **2020**.
22. Epstein, A. K.; Wong, T.-S.; Belisle, R. A.; Boggs, E. M.; Aizenberg, J., Liquid-infused structured surfaces with exceptional anti-biofouling performance. *Proceedings of the National Academy of Sciences* **2012**, *109* (33), 13182-13187.

23. Wilson, P. W.; Lu, W.; Xu, H.; Kim, P.; Kreder, M. J.; Alvarenga, J.; Aizenberg, J., Inhibition of ice nucleation by slippery liquid-infused porous surfaces (SLIPS). *Phys Chem Chem Phys* **2013**, *15* (2), 581-5.
24. Bocquet, L.; Quéré, D.; Witten, T. A.; Cugliandolo, L. F., *Soft Interfaces: Lecture Notes of the Les Houches Summer School: Volume 98, July 2012*. Oxford University Press: 2017; Vol. 98.
25. Bell, J. M.; Cameron, F., The flow of liquids through capillary spaces. *The Journal of Physical Chemistry* **2002**, *10* (8), 658-674.
26. Berg, J. C., *An introduction to interfaces & colloids: the bridge to nanoscience*. World Scientific: 2010.
27. Washburn, E. W., The dynamics of capillary flow. *Physical Review B* **1921**, *17* (3), 273.
28. Kim, J.; Moon, M. W.; Kim, H. Y., Dynamics of hemiwicking. *Journal of Fluid Mechanics* **2016**, *800*, 57-71.
29. Srivastava, N.; Din, C. S.; Judson, A.; MacDonald, N. C.; Meinhart, C. D., A unified scaling model for flow through a lattice of microfabricated posts. *Lab on a Chip* **2010**, *10* (9), 1148-1152.
30. Xiao, R.; Enright, R.; Wang, E. N., Prediction and optimization of liquid propagation in micropillar arrays. *Langmuir* **2010**, *26* (19), 15070-5.
31. Xiao, R.; Wang, E. N., Microscale liquid dynamics and the effect on macroscale propagation in pillar arrays. *Langmuir* **2011**, *27* (17), 10360-4.
32. Krishnan, S. R.; Bal, J.; Putnam, S. A., A simple analytic model for predicting the wicking velocity in micropillar arrays. *Scientific Reports* **2019**, *9* (1), 1-9.
33. Smith, J. D.; Dhiman, R.; Anand, S.; Reza-Garduno, E.; Cohen, R. E.; McKinley, G. H.; Varanasi, K. K., Droplet mobility on lubricant-impregnated surfaces. *Soft Matter* **2013**, *9* (6), 1772-1780.
34. Bico, J.; Tordeux, C.; Quere, D., Rough wetting. *Europhys Lett* **2001**, *55* (2), 214-220.
35. Hay, K.; Dragila, M.; Liburdy, J., Theoretical model for the wetting of a rough surface. *Journal of colloid and interface science* **2008**, *325* (2), 472-477.
36. Mai, T. T.; Lai, C. Q.; Zheng, H.; Balasubramanian, K.; Leong, K. C.; Lee, P. S.; Lee, C.; Choi, W. K., Dynamics of wicking in silicon nanopillars fabricated with interference lithography and metal-assisted chemical etching. *Langmuir* **2012**, *28* (31), 11465-71.
37. Krüger, T.; Kusumaatmaja, H.; Kuzmin, A.; Shardt, O.; Silva, G.; Viggien, E. M., The lattice Boltzmann method. *Springer International Publishing* **2017**, *10* (978-3), 4-15.
38. Blow, M. L.; Yeomans, J. M., Anisotropic imbibition on surfaces patterned with polygonal posts. *Philosophical Transactions of the Royal Society A: Mathematical, Physical and Engineering Sciences* **2011**, *369* (1945), 2519-2527.
39. Kim, J.; Moon, M.-W.; Lee, K.-R.; Mahadevan, L.; Kim, H.-Y., Hydrodynamics of writing with ink. *Physical Review Letters* **2011**, *107* (26), 264501.

TOC Graphic



Predicting Hemiwicking Dynamics on Textured Substrates

Bharath Natarajan,[§] Aditya Jaishankar,[§] Mark King,[§] Fandi Oktasendra,^{||#} Samuel J. Avis,^{||} Andrew R Konicek,[§] Garrett Wadsworth,[§] Arben Jusufi,[§] Halim Kusumaatmaja,^{||} Mohsen S Yeganeh[§]

[§]Corporate Strategic Research, ExxonMobil Research and Engineering, 1545 U.S. 22, Annandale, New Jersey 08801, United States

^{||}Department of Physics, Durham University, Durham, DH1 3LE, United Kingdom

[#]Department of Physics, Universitas Negeri Padang, Padang 25131, Indonesia

Supporting Information

Model Development

The energetic criterion for the hemiwicking of micropillar arrays was derived by Bico et al. as follows.¹ Consider a micropillar array of roughness factor r , which is the ratio of the real area of the surface, A_r to the area of the surface when projected onto a 2D plane, A_p . The area of the top surface of the pillars is A_t . By definition, in the purely imbibed state, the top of the pillars remain dry.^{2, 3} This dry fraction of the projected area A_t/A_p is labeled φ_s (Figure 1). When such an array,

of unit area into the page, is brought into contact with a liquid reservoir, the change in interfacial energy for a propagation distance dz can be written as (2)

$$dE = E_{wet} - E_{dry} \quad (1)$$

$$dE = (\gamma_{LV}(1 - \varphi_s)dz + \gamma_{SL}(r - \varphi_s)dz + \gamma_{SV}\varphi_s dz) - (\gamma_{SV} \cdot r \cdot dz) \quad (2)$$

$$dE = (\gamma_{SL} - \gamma_{SV})(r - \varphi_s)dz + \gamma_{LV}(1 - \varphi_s)dz \quad (3)$$

where, γ_{LV} , γ_{SV} and γ_{SL} are the liquid-vapor, solid-vapor and solid-liquid surface energies respectively. Using Young's equation

$$\gamma_{SV} = \gamma_{SL} + \gamma_{LV}\cos\theta \quad (4)$$

where, θ is the equilibrium contact angle, equation (3) may be rewritten as

$$dE = -\gamma_{LV} \cos \theta (r - \varphi_s)dz + \gamma_{LV}(1 - \varphi_s)dz \quad (5)$$

In order for the imbibition of liquid to be energetically favored, $dE \leq 0$. This means

$$\cos \theta \geq \frac{(1 - \varphi_s)}{(r - \varphi_s)} = \cos \theta_c \quad (6)$$

In these systems, when the hemiwicking criterion (6) is satisfied, and the rate of imbibition of liquid into the texture is simply dictated by the balance between a driving capillary pressure (ΔP_L) and a dissipative Darcy-like viscous pressure (ΔP_V). The interplay between these forces results in a diffusion-like scaling for the imbibition distance, known as the Washburn law.⁴

$$z = (Dt)^{0.5} \quad (7)$$

where, D is a hemiwicking coefficient and t is time.

The capillary pressure (ΔP_L) is the change in energy per unit volume of liquid imbibed ($-dE/dV$).

We recognize that dV for a propagation distance dz and pillar height h is

$$dV = (1 - \varphi_s)h \cdot dz \quad (8)$$

Combining (5) and (8), we get

$$\Delta P_L = -\frac{dE}{dV} = \frac{\gamma_{LV} \cos \theta (r - \varphi_s)}{(1 - \varphi_s)h} - \frac{\gamma_{LV}}{h} \quad (9)$$

Using (6), (9) can be written as

$$\Delta P_L = \frac{\gamma_{LV}}{h} \left(\frac{\cos \theta - \cos \theta_c}{\cos \theta_c} \right) \quad (10)$$

As is evident, the capillary pressure is only positive when the $\theta \leq \theta_c$. In other scenarios, there is no driving force for hemiwicking. The viscous dissipation force per unit area or viscous pressure (ΔP_V) can be estimated from a modification to the classical Poiseuille law for a liquid film of thickness h flowing on a plane.¹

$$\Delta P_V = \frac{3\mu v z}{h^2} \beta \quad (11)$$

where, μ is the viscosity of the liquid, v is the velocity of propagation (dz/dt) and β is a correction factor to the classical Poiseuille law that accounts for enhanced dissipative contributions from the microtexture. The thickness h here is the same as the pillar height, as during hemiwicking the top of the liquid volume is pinned/confined to the top edge of the pillar.² In the beginning of imbibition, i.e., when hydrostatic pressure is negligible, balancing the capillary pressure and viscous pressures we get

$$\frac{\gamma_{LV}}{h} \left(\frac{\cos \theta - \cos \theta_c}{\cos \theta_c} \right) = \frac{3\mu v z}{h^2} \beta \quad (12)$$

Rearranging (12),

$$v = \frac{dz}{dt} = \frac{\gamma_{LV} h}{3\mu z} \left(\frac{\cos \theta - \cos \theta_c}{\cos \theta_c} \right) \frac{1}{\beta} \quad (13)$$

$$z \cdot dz = \frac{\gamma_{LV} h}{3\mu} \left(\frac{\cos \theta - \cos \theta_c}{\cos \theta_c} \right) \frac{1}{\beta} \cdot dt \quad (14)$$

Integrating (14),

$$z^2 = \frac{2\gamma_{LV} h}{3\mu} \left(\frac{\cos \theta - \cos \theta_c}{\cos \theta_c} \right) \frac{1}{\beta} \cdot t \quad (15)$$

Comparing (7) and (15), the hemiwicking coefficient is found to be

$$D = \frac{2\gamma_{LV} h}{3\mu} \left(\frac{\cos \theta - \cos \theta_c}{\cos \theta_c} \right) \frac{1}{\beta} \quad (15)$$

To get β , we approximate the flow of liquid through the micropillar array as flow through an equivalent microchannel of the same height and unit cell size (Figure 1b). However, the width, w of the channel needs to be modified in order that the viscous dissipation between systems remains identical. This can be achieved by equating the volume available for flow between the two systems. The rationale behind this approximation is explained below.

Consider Darcy's law (16), which relates the volume flux in a porous material to the pressure gradient.

$$Q = \frac{kA}{\mu} \frac{dp}{dx} \quad (16)$$

where, Q is the volume flow per time, A is the cross-sectional area of the material, dp/dx is the pressure gradient and k is the permeability. The term $\frac{kA}{\mu}$ is called the hydraulic resistance (as flux and pressure gradient are fully equivalent to current and voltage in Ohm's law, respectively). For our equivalent systems, the velocity, Q/A , will need to be the identical. Since the driving force for spontaneous imbibition is the capillary pressure, the pressure gradient between the systems is set to be identical. Thus, for equivalence, our approximation needs to ensure that the permeability between the systems is also identical. Now consider a porous medium, of cross-sectional area A , comprised of N parallel pipes, of radius b , whose axes are misaligned with the length direction (Figure S1a). In other words the flow path through this medium, L_e , is larger than the length L . The flux through this medium is given by

$$Q = \frac{N\pi b^4}{8\mu} \frac{\Delta p}{L_e} \quad (17)$$

where Δp is the pressure gradient. Recognizing, tortuosity, τ , as L_e/L , and porosity, ϕ , as $\frac{N\pi b^2 L_e}{AL}$, we get

$$Q = \frac{A b^2 \phi}{\mu 8\tau^2} \frac{\Delta p}{L} = \frac{A b^2 \phi}{\mu 8\tau^2} \frac{dp}{dx} \quad (18)$$

Comparing (18) with (16), we see that

$$k \sim C \frac{b^2 \phi}{\tau^2} \quad (19)$$

where C is a pre-factor that varies minimally between 0.3 and 0.4, and will henceforth be neglected.⁵ We introduce a new term hydraulic radius, R_h , which is defined as the pore volume, V_p , over the solid-liquid interaction area during the flow, A_{sl} ,

$$R_h = \frac{V_p}{A_{sl}} = \frac{\pi b^2 L_e}{2\pi b L_e} = \frac{b}{2} \quad (20)$$

Substituting (20) into (19), we get

$$k \sim \frac{R_h^2 \phi}{4\tau^2} \quad (21)$$

Thus for the two systems to have the same permeability, they need to have identical $\frac{R_h^2 \phi}{\tau^2}$, values.

This relationship is observed to be relatively robust for various geometries.⁵ In (21), τ is typically dependent on ϕ . The relationship between these terms is given by the Archie law as

$$\tau \sim \phi^{-m} \quad (22)$$

where m is a real number, typically greater than or equal to 1. Thus, from (22) and (21), we observe that

$$k \sim R_h^2 \phi^{2m+1} \quad (23)$$

Now, since R_h is V_p/A_{sl} , and since porosity is the pore volume over the total volume (V_t),

$$k \sim \frac{V_p^{2m+3}}{A_{sl}^2} \frac{1}{V_t^{2m+1}} \quad (24)$$

Since we set the same unit cell size and height between the channel and the pillar array, the total volume, V_t , is identical between the systems. Thus for equivalence, the necessary condition is

$$\frac{V_{p,ch}^{2m+3}}{A_{sl,ch}^2} = \frac{V_{p,array}^{2m+3}}{A_{sl,array}^2} \quad (25)$$

In (25), the equivalence criterion is more strongly reliant on the volume of the channel than the solid-liquid interaction area, as the volume term is to a much higher. For this reason, it is possible to simply approximate the equivalence by forcing the systems to have identical volumes. To demonstrate this quantitatively, we calculate the width of the channel, w , for various values of m , and plot them against w calculated using the identical volume approximation in Figure S1b. Here, we find the w values to be very similar (slope ~ 1), thereby validating our approach.

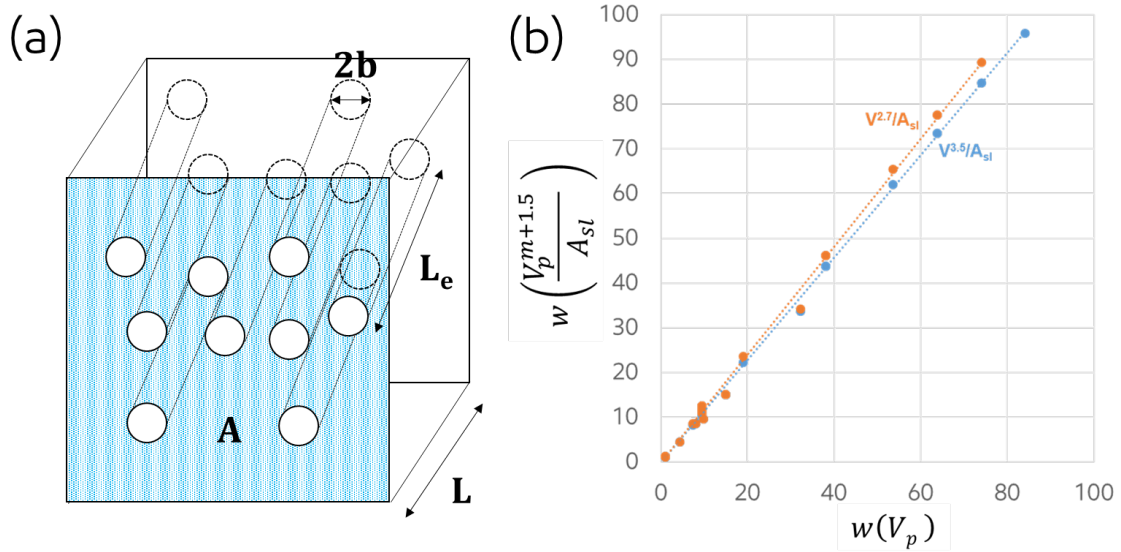


Figure S1. (a) Illustration of porous system employed to derive the relationship between permeability and pore geometry. (b) Plot of w calculated for various values of m versus w calculated assuming that the pore volume i.e., volume available for flow is constant.

With the equivalence established, the velocity of the liquid through the microchannel can be obtained by solving Navier-Stokes' equation for steady state, parallel, incompressible flow.

$$-\frac{\Delta P_L}{\mu z} = \frac{\partial^2 U}{\partial x^2} + \frac{\partial^2 U}{\partial y^2} \quad (26)$$

where $U(x, y)$ is the velocity profile in the microchannel. Since the term on the left hand side is independent of x and y , we start by solving Laplace's equation

$$\frac{\partial^2 U}{\partial x^2} + \frac{\partial^2 U}{\partial y^2} = 0 \quad (27)$$

Using the method of separation of variables

$$U(x, y) = X(x)Y(y), \quad U(x, y) = \sum_{n=0}^{\infty} X(x)Y(y) \quad (28)$$

Substituting (28) into (27)

$$\frac{\partial^2 X}{\partial x^2} = -\frac{\partial^2 Y}{\partial y^2} = \lambda \quad (29)$$

where, λ is a constant. Now solving for Y

$$\frac{\partial^2 Y}{\partial y^2} + \lambda Y = 0 \quad (30)$$

The standard solution to (30) is

$$Y = c_1 \sin(\sqrt{\lambda}y) + c_2 \cos(\sqrt{\lambda}y) \quad (31)$$

Assuming no slip on the microchannel walls, we have the boundary condition $U(x, y = \pm h) = 0$, i.e., $Y(\pm h) = 0$ (Figure 1b). Solving equation (31) with the boundary condition in mind, we get

$$Y = c_2 \cos\left(\frac{(2n+1)\pi}{2h}y\right) \quad (32)$$

$$U(x, y) = \sum_{n=0}^{\infty} X(x) \cos\left[\frac{(2n+1)\pi y}{2h}\right] \quad (33)$$

Now we expand the left hand side of (26) into a Taylor series

$$-\frac{\Delta P_L}{\mu z} = \sum_{n=0}^{\infty} B_n \cos\left[\frac{(2n+1)\pi y}{2h}\right] \quad (34)$$

Multiplying (24) by $\cos\left[\frac{(2m+1)\pi y}{2h}\right]$ and integrating from $-h$ to h we get

$$\int_{-h}^h -\frac{\Delta P_L}{\mu z} \cos\left[\frac{(2m+1)\pi y}{2h}\right] dy = \int_{-h}^h B_m \cos\left[\frac{(2m+1)\pi y}{2h}\right]^2 dy \quad (35)$$

$$-\frac{\Delta P_L}{\mu z} \frac{2h}{(2m+1)\pi y} (-1)^m = \frac{(2m+1)\pi y}{2h} B_m h \quad (36)$$

$$B_m = -\frac{4\Delta P_L}{\mu z (2m+1)\pi} (-1)^m \quad (37)$$

$$-\frac{\Delta P_L}{\mu z} = -\frac{4\Delta P}{\mu z \pi} \sum_{n=0}^{\infty} \frac{(-1)^m}{(2n+1)} \cos\left[\frac{(2n+1)\pi y}{2h}\right] \quad (38)$$

Substituting (38) and (33) into Navier-Stokes' equation (16), we get

$$\begin{aligned} & -\frac{4\Delta P_L}{\mu z \pi} \sum_{n=0}^{\infty} \frac{(-1)^m}{(2n+1)} \cos\left[\frac{(2n+1)\pi y}{2h}\right] \\ & = \sum_{n=0}^{\infty} \left[X''(x) - \left[\frac{(2n+1)\pi y}{2h}\right]^2 X(x) \right] \cos\left[\frac{(2n+1)\pi y}{2h}\right] \end{aligned} \quad (39)$$

i.e.,

$$-\frac{4\Delta P_L}{\mu z \pi} \frac{(-1)^m}{(2n+1)} = \left[X''(x) - \left[\frac{(2n+1)\pi y}{2h} \right]^2 X(x) \right] \quad (40)$$

We now need to solve for $X(x)$. We split $X(x)$ into a homogenous and inhomogeneous component.

$$X(x) = X_{hom}(x) + X_{inhom}(x) \quad (41)$$

Solving for the homogenous part, we get

$$X_{hom}''(x) - \left[\frac{(2n+1)\pi y}{2h} \right]^2 X_{hom}(x) = 0 \quad (42)$$

The solution to X_{hom} here is

$$X_{hom}(x) = D \cosh \left[\frac{(2n+1)\pi x}{2h} \right] \quad (43)$$

Using (43), (41) in (40)

$$X_{inhom} = \frac{16\Delta P_L}{\mu z} \frac{(-1)^m h^2}{(2n+1)^3 \pi^3} \quad (44)$$

Therefore

$$X(x) = D \cosh \left[\frac{(2n+1)\pi x}{2h} \right] + \frac{16\Delta P_L}{\mu z} \frac{(-1)^m h^2}{(2n+1)^3 \pi^3} \quad (45)$$

Assuming no slip on the microchannel walls, we have the boundary condition $U(\pm w/2, y) = 0$,

i.e., $X(\pm w/2) = 0$ (Figure 1b). Solving equation (45) with this boundary condition, we get

$$X(x) = \frac{16\Delta P_L}{\mu z} \frac{(-1)^m h^2}{(2n+1)^3 \pi^3} \left(1 - \frac{\cosh \left[\frac{(2n+1)\pi x}{2h} \right]}{\cosh \left[\frac{(2n+1)\pi w}{4h} \right]} \right) \quad (46)$$

From (46) and (33), we get the velocity profile in the microchannel

$$U(x, y) = \frac{16\Delta P_L h^2}{\mu z \pi^3} \sum_{n=0}^{\infty} \frac{(-1)^n}{(2n+1)^3} \left(1 - \frac{\cosh \left[\frac{(2n+1)\pi x}{2h} \right]}{\cosh \left[\frac{(2n+1)\pi w}{4h} \right]} \right) \cos \left[\frac{(2n+1)\pi y}{2h} \right] \quad (47)$$

Lattice Boltzmann Simulation Validation

To confirm that the Eq. (14) in the main text represents the appropriate equation for mean velocity through a rectangular channel, we perform LB simulations of flow through rectangular channels of various geometries and compare the simulated D against that predicted by Eq. (14). The agreement between the simulated and predicted values, shown in Figure S2, validates the expression in Eq. (14).

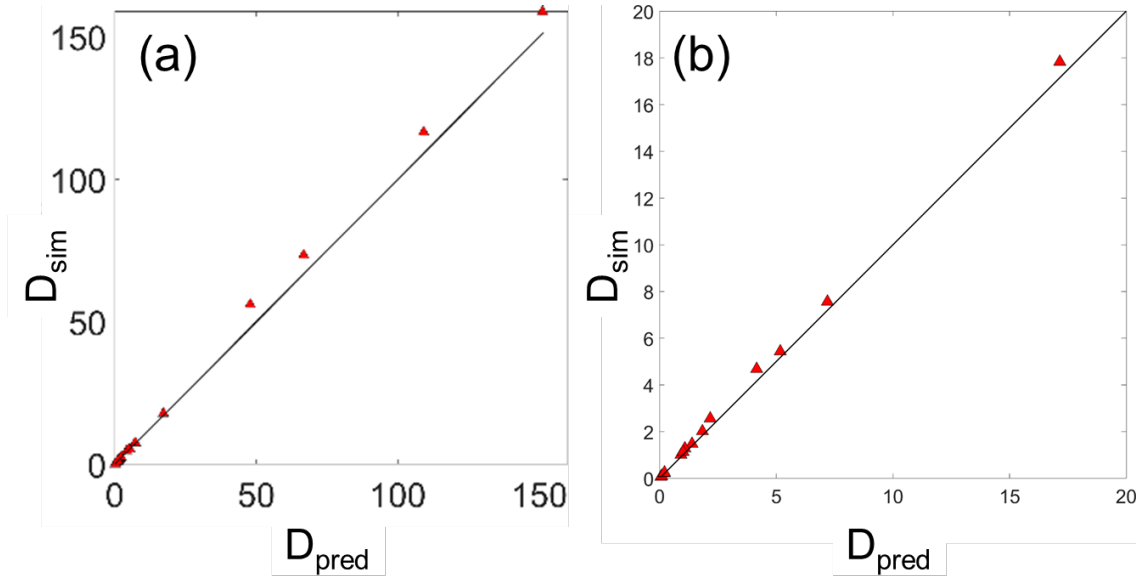


Figure S2. (b) Plot of hemiwicking coefficients, D , for grooves calculated from Lattice Boltzmann simulations vs. those calculated using analytical expression in (14). Inset shows comparison out to higher D values.

Figure S3 shows the comparison between D values calculated from lattice Boltzmann simulations and those measured experimentally as tabulated in Table S1. It can be seen that the simulated D values are in excellent agreement with experimental data, especially for p/d values between 3.3 and 4, and the p/h values between 0.14 and 3.3 (sparse arrays). Some deviations are observed for p/d values are close to 1 (very dense arrays), consistent with the results shown in Fig. 4 of the main text.

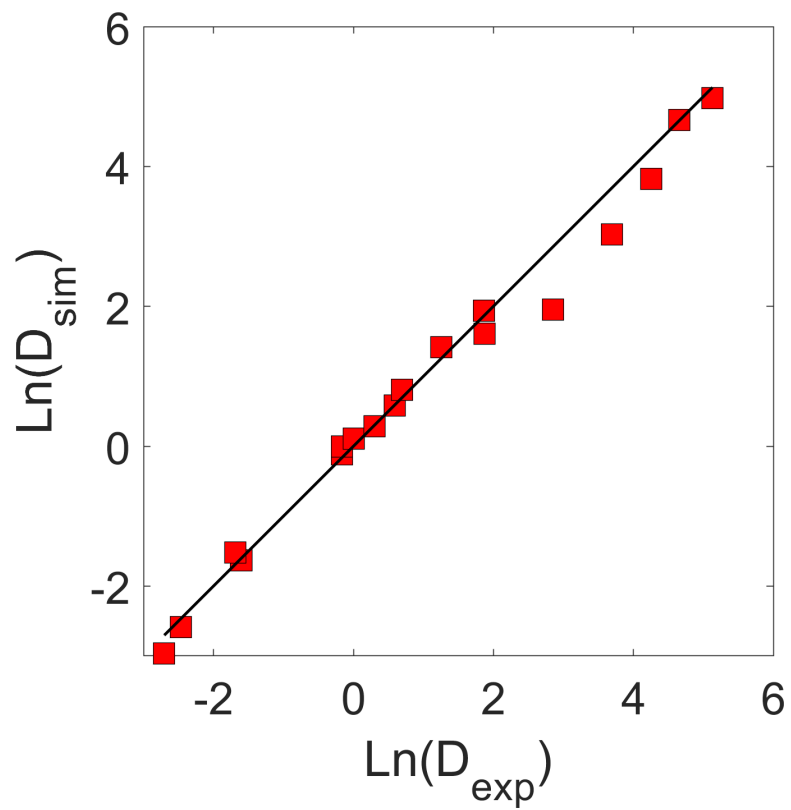


Figure S3. Plot of natural logarithm of D obtained from LB simulations *versus* natural logarithm of experimentally measured D reported in literature.

Equations for square and cylindrical arrays.

The equation (16) in the main text is agnostic to the geometry of the texture. However it may be extended to various geometries using suitable substitution. For example for a square array of cylindrical pillars,

with $\cos \theta_c = \frac{(p^2 - d^2)}{(p^2 + 4dh - d^2)}$, and $w = (p^2 - d^2)/p$, Eq. (16) from the main text takes the form

$$D = \frac{2\gamma_{LV}h}{3\mu} \left(\frac{\cos \theta (p^2 + \pi dh - \pi d^2/4)}{(p^2 - \pi d^2/4)} - 1 \right) \left(1 - \frac{4ph}{\pi(p^2 - \pi d^2/4)} \tanh \left[\frac{\pi(p^2 - \pi d^2/4)}{4ph} \right] \right) \quad (48)$$

where, d is the pillar diameter and p is the unit cell size (or pitch). For a square array of square cross-section pillars, with $\cos \theta_c = \frac{(p^2 - \pi d^2/4)}{(p^2 + \pi dh - \pi d^2/4)}$, and $w = (p^2 - \pi d^2/4)/p$, Eq. (16) from the main text

takes the form

$$D = \frac{2\gamma_{LV}h}{3\mu} \left(\frac{\cos \theta (p^2 + 4dh - d^2)}{(p^2 - d^2)} - 1 \right) \left(1 - \frac{4ph}{\pi(p^2 - d^2)} \tanh \left[\frac{\pi(p^2 - d^2)}{4ph} \right] \right) \quad (49)$$

where, d is the side of the square cross-section, p is the unit cell size (or pitch).

Table S2. A tabulation of hemiwicking models with proposed analytical expressions for the hemiwicking coefficient, conditions where expressions are applicable and parameter proposed to best fit experimental data.

Model	Equation	Condition	Fitting Parameter	Average Absolute Error
Bico <i>et al.</i> ¹	$D = \frac{\gamma_{LV}h}{\mu} \left(\frac{\frac{\pi dh}{b^2}}{1 - \frac{\pi}{4} \left(\frac{d}{p}\right)^2} \right)$	-	-	6.03
Ishino <i>et al.</i> ⁶	$D = \frac{\gamma_{LV}d}{\mu} \left(\frac{h}{p}\right)^2$	$p \gg h$	-	11.57
	$D = \frac{\gamma_{LV}d}{\mu} \left(\ln\left(\frac{2p}{d}\right) - 1.31\right)$	$p \ll h$ $\theta = 0^\circ$	-	0.59
Srivastava <i>et al.</i> ⁷	$D = \frac{\gamma_{LV}}{\mu} \frac{d^{0.5}h^{0.17}(p-d)^{1.33}}{p\left[1 - \frac{\pi}{4}\left(\frac{d}{p}\right)^2\right]}$	$\theta = 0^\circ$	$\frac{\pi}{15}$	2.44
Kim <i>et al.</i> ^{2*}	$D = \frac{\gamma_{LV}h}{\mu} \left(\frac{r-1}{1+h(r-1)/p}\right)$	$\theta = 0^\circ$	~ 0.24	3.96 (0.33 with fitting parameter)
Kim <i>et al.</i> ^{8*}	$D = \frac{\gamma_{LV}h}{\mu} (1 - 1/r)$	$\theta = 0^\circ$	-	3.45
Krishnan <i>et al.</i> ^{9,}	$D = \frac{2\gamma_{LV}}{\mu} \frac{hp(p-d)(r-1)^{0.5}}{x_o^2}$	$\theta = 0^\circ$	$\sim 1/95$	0.79 with fitting parameter

* $r = 1 + \frac{\pi dh}{p^2}$

|| $x_o = \frac{hp}{\pi d}$

Table S1. A tabulation of experimental data used for model validation.

Source	Theta (degrees)	Height (μm)	Diameter (μm)	Pitch (μm)	Viscosity (mPa.s)	γ_{LV} (mN/m)	D (mm^2/s)
Mai et al. ¹⁰	18	0.75	0.275	1	39.4	33.99	0.07
	18	7	0.3	1	39.4	33.99	0.17
	18	4.2	0.3	1	39.4	33.99	0.13
	18	2	0.3	1	39.4	33.99	0.08
Ishino et al. ⁶	0	26	2.6	10	97	20	0.19
	0	26	2.6	10	48	20	0.32
	0	26	2.6	10	19	20	1.00
	0	26	2.6	10	9.5	20	2.00
	0	26	2.6	10	4.6	20	3.55
	0	18	2.6	10	97	20	0.15
	0	18	2.6	10	48	20	0.30
	0	18	2.6	10	19	20	1.80
	0	14	2.6	10	97	20	0.20
	0	14	2.6	10	48	20	0.32
	0	14	2.6	10	19	20	0.85
	0	14	2.6	10	9.5	20	1.55
	0	14	2.6	10	4.6	20	3.50
	0	10	2.6	10	48	20	0.30
	0	10	2.6	10	19	20	0.85
	0	10	2.6	10	9.5	20	1.80
	0	10	2.6	10	4.6	20	2.90
	0	6	2.6	10	97	20	0.10
	0	6	2.6	10	48	20	0.20
	0	6	2.6	10	19	20	0.55
	0	6	2.6	10	9.5	20	1.35
	0	6	2.6	10	4.6	20	1.80
	0	4	2.6	10	48	20	0.13
	0	4	2.6	10	19	20	0.40
0	4	2.6	10	9.5	20	0.70	
0	4	2.6	10	4.6	20	1.15	
Xiao et al. ^{11, 12}	38	8.3	2.82	8.1	1	72	70.56
	38	8.3	2.9	5.5	1	72	40.14
	10	17	5	10	1	72	74.13
	10	17	5	20	1	72	105.27
CSR	0	7	10	20	43.8	29.5	0.59
	10	7	10	20	8.8	28	3.00
	5	7	10	20	3	26.6	17.28
Kim et al. ²	0	26	10	40	1.3	72.8	169.00
	0	26	10	40	18	48	6.45
	0	26	10	75	18	48	1.77
	0	26	10	85	18	48	1.14

1. Bico, J.; Thiele, U.; Quere, D., Wetting of textured surfaces. *Colloid Surface A* **2002**, *206* (1-3), 41-46.
2. Kim, J.; Moon, M. W.; Kim, H. Y., Dynamics of hemiwicking. *Journal of Fluid Mechanics* **2016**, *800*, 57-71.
3. Smith, J. D.; Dhiman, R.; Anand, S.; Reza-Garduno, E.; Cohen, R. E.; McKinley, G. H.; Varanasi, K. K., Droplet mobility on lubricant-impregnated surfaces. *Soft Matter* **2013**, *9* (6), 1772-1780.
4. Washburn, E. W., The dynamics of capillary flow. *Physical Review B* **1921**, *17* (3), 273.
5. Paterson, M., The equivalent channel model for permeability and resistivity in fluid-saturated rock—a re-appraisal. *J Mechanics of Materials* **1983**, *2* (4), 345-352.
6. Ishino, C.; Reyssat, M.; Reyssat, E.; Okumura, K.; Quere, D., Wicking within forests of micropillars. *Epl-Europhys Lett* **2007**, *79* (5).
7. Srivastava, N.; Din, C. S.; Judson, A.; MacDonald, N. C.; Meinhart, C. D., A unified scaling model for flow through a lattice of microfabricated posts. *Lab on a Chip* **2010**, *10* (9), 1148-1152.
8. Kim, J.; Moon, M.-W.; Lee, K.-R.; Mahadevan, L.; Kim, H.-Y., Hydrodynamics of writing with ink. *Physical Review Letters* **2011**, *107* (26), 264501.
9. Krishnan, S. R.; Bal, J.; Putnam, S. A., A simple analytic model for predicting the wicking velocity in micropillar arrays. *Scientific Reports* **2019**, *9* (1), 1-9.
10. Mai, T. T.; Lai, C. Q.; Zheng, H.; Balasubramanian, K.; Leong, K. C.; Lee, P. S.; Lee, C.; Choi, W. K., Dynamics of wicking in silicon nanopillars fabricated with interference lithography and metal-assisted chemical etching. *Langmuir* **2012**, *28* (31), 11465-71.
11. Xiao, R.; Enright, R.; Wang, E. N., Prediction and optimization of liquid propagation in micropillar arrays. *Langmuir* **2010**, *26* (19), 15070-5.
12. Xiao, R.; Wang, E. N., Microscale liquid dynamics and the effect on macroscale propagation in pillar arrays. *Langmuir* **2011**, *27* (17), 10360-4.